Composites Part B 223 (2021) 109130

Contents lists available at ScienceDirect

Composites Part B

journal homepage: www.elsevier.com/locate/compositesb

BODIPY coated on MXene nanosheets for improving mechanical and fire safety properties of ABS resin

San-E Zhu [a,1], Fen-Dou Wang [a,1], Jun-Jie Liu [a], Li-Li Wang [a], Cheng Wang [b], Anthony Chun Yin Yuen [b,**], Timothy Bo Yuan Chen [b], Imrana I. Kabir [b], Guan Heng Yeoh [b], Hong-Dian Lu [a], Wei Yang [a,*]

[a] School of Energy, Materials and Chemical Engineering, Hefei University, 99 Jinxiu Avenue, Hefei, Anhui, 230601, PR China
[b] School of Mechanical and Manufacturing Engineering, University of New South Wales, Sydney, NSW, 2052, Australia

ARTICLE INFO

Keywords:
MXene
BODIPY
ABS resin
Mechanical properties
Flame retardant

ABSTRACT

Acrylonitrile-butadiene-styrene (ABS) resin is a commonly used engineering thermoplastic. Nevertheless, the fire toxicity hazards (HCN, NO_x, NH_3 and CO) generated from the combustion of ABS remains a major concern, especially in building fire scenarios. To address this issue, boron dipyrromethene (BODIPY) modified MXene ($Ti_3C_2T_x$) nanosheets were prepared and utilized as a flame retardant for ABS. The loading of 0.5 wt% BODIPY-MXene resulted in the uniform dispersion in ABS. Accordingly, the tensile strength, Young's modulus and elongation at break of ABS/BODIPY-MXene0.5 were improved by 27.8%, 18.6% and 17.9% respectively compared to neat ABS, suggesting the enhanced mechanical properties. The limiting oxygen index (LOI) value was increased from 19.5% for neat ABS to 21.5% and 23.5% for ABS/BODIPY-MXene0.5 and ABS/BODIPY-MXene2.0 benefitted from the rapid carbonization. The cone calorimeter coupled with FTIR analysis showed that the reductions in peak heat release rate (−24.5%), peak smoke production rate (−18.4%), peak concentration of HCN (−33.5%), NO (−22.0%), N_2O (−46.6%), NH_3 (−76.0%) and CO (−28.8%) were achieved by incorporating 0.5 wt% BODIPY-MXene to ABS in comparison with pure ABS. The improved fire safety properties were primarily attributed to the excellent barrier, free radical capture, and catalytic carbonization effect of BODIPY-MXene nanosheets within ABS matrix.

1. Introduction

ABS resin has been commonly utilized as engineering thermoplastic for multiple industrial and domestic applications owing to its excellent mechanical performance, outstanding chemical resistance and ease of processing [1–3]. However, ABS is highly flammable with a low LOI of 17–19%. Furthermore, the melting point of ABS is low and its combustion leads to the generation of high intensity flames, dripping fire debris, soot particles, as well as toxic gases (i.e. HCN, NO_x, NH_3 and CO), which are extremely harmful to human health [4,5]. Halogen- and phosphorus-based flame retardants, including decabromodiphenyl oxide [6,7], polyphosphates [8–10], phosphinate [5,11,12], hypophosphite [13,14] and DOPO derivatives [15,16], can effectively reduce the heat release of ABS via gas- and/or condensed-phase flame retardant mechanism, yet the reduction in smoke and toxicity hazards are found to be insignificant.

Nanoparticles, such as nanoclay [17–19], carbon nanotubes (CNTs) [18,20,21], layered double hydroxides [22–24], graphene [24–28], have attracted extensive attention due to their flame retardant and smoke suppression effect for ABS. Generally, untreated nanoparticles tend to self-aggregate leading to the heterogeneous dispersion in polymers. Chemical functionalization is a suitable approach to address this issue. Ma et al. [21] prepared functionalized CNTs grafted with intumescent flame retardant, which was shown to reduce the peak heat release rate (PHRR) and average specific extinction area (ASEA) of ABS. Zhang et al. [23] carried out the intercalation of perfluorobutane sulfonate (PFBS) into ZnMgAl-LDH. The flammability tests demonstrated that ABS/ZnMgAl-PFBS-LDH possessed superior flame retardancy and

* Corresponding author.
** Corresponding author.
E-mail addresses: c.y.yuen@unsw.edu.au (A.C.Y. Yuen), yangwei@hfuu.edu.cn (W. Yang).
[1] San-E Zhu and Fen-Dou Wang contributed equally to this work (co-first author).

https://doi.org/10.1016/j.compositesb.2021.109130
Received 16 May 2021; Received in revised form 30 June 2021; Accepted 6 July 2021
Available online 9 July 2021

Table 1
Fire and smoke hazards of ABS nanocomposites in the reported work.

Sample	Filler loading	PHRR[a]	Smoke	Ref.
ABS/MWNT	0.5 wt%	−44.4%	−32.3% [b]	[21]
ABS/MWNT-PDSPB	0.5 wt%	−51.3%	−19.7% [b]	[21]
ABS/ZnMgAl–NO_3-LDH	2.0 wt%	/	−0.3% [c]	[23]
ABS/ZnMgAl-PFBS-LDH	2.0 wt%	/	−6.5% [c]	[23]
ABS/GNS	2.0 wt%	+1.4%	−6.7% [b]	[25]
ABS/RGO1	1.0 wt%	−8.2%	−19.1% [d]	[26]
ABS/PN-RGO1	1.0 wt%	−19.0%	−27.6% [d]	[26]
ABS/La@PN-RGO1	1.0 wt%	−38.5%	−43.8% [d]	[26]
ABS/SbMo-BrG0.5	0.5 wt%	−16.2%	−26.1% [d]	[27]
ABS/SbMo-BrG0.1	1.0 wt%	−28.4%	−45.2% [d]	[27]
ABS/Mo5/PN-rGO	1.0 wt%	−50.7%	−60.3% [d]	[28]

[a] Reduction of peak heat release rate (PHRR).
[b] Reduction of average specific extinction area (ASEA).
[c] Reduction of smoke density.
[d] Reduction of peak smoke production rate (PSPR).

smoke suppression properties compared to ABS/ZnMgAl–NO_3-LDH. Huang et al. [26–28] fabricated a series of functionalized graphene nanosheets (f-GNS) by using phosphorus-, bromine- and metal-based compounds for reducing the heat release and toxic fumes of ABS. Compared to the undecorated GNS, the improvement of fire safety performance for f-GNS was more significant, which was principally attributed to the interface catalysis carbonization (i.e. charring of organophosphorus, rare earth and Sb/Br system) [25–28]. Additionally, two-dimensional (2D) nano-fillers with surface engineering show more remarkable smoke suppression compared to 1D CNTs (see Table 1), because of the unique sheet barrier effect from layered nanomaterials. Despite the huge achievement, incorporating nano-fillers to ABS for reducing toxicity hazards have yet to be reported.

MXenes (transition metal carbides and/or nitrides), a new generation of 2D nanomaterials, have drawn enormous research interest due to their outstanding conductivity [29], tunable terminal groups [30] and intercalation ability [31]. MXene ($Ti_3C_2T_x$) (<5 wt%) has exhibited its exceptional effectiveness as a multifunctional additive that significantly improves the mechanical, thermal, conductivity, gas barrier and flame retardant properties of a range of polymers [32–39]. In our previous works [36–38], the surface modification of MXene nanosheets using organics (i.e. alkyl ammonium bromide, tetrabutyl phosphine chloride and POSS) based on charge attraction was successfully implemented. The introduction of 2.0 wt% functionalized MXenes into polymers (i.e. TPU, PS) showed effective inhibition on heat release and toxic fumes, including smoke and CO, owing to the barrier effect and interface catalysis carbonization. Nevertheless, the fragility will improve if the concentration of nano-fillers increases due to self-aggregation [34–36]. Consequently, this work aims to significantly reduce the thermal and non-thermal hazards of ABS with a minimal amount of MXene loading.

Boron dipyrromethene (BODIPY), a fluorochrome with high extinction coefficient, outstanding bio-compatibility, good thermal and photochemical stability, is commonly used as bio-labeling [40], photodynamic therapy [41] and dye-sensitized solar cell [42]. Owing to the unique chemical structure composed of multiple elements (i.e. F, B, N), BODIPY is a good option for fire retardant applications. In this work, BODIPY was utilized as a modifier to decorate MXene nanosheets on the basis of charge attraction between amino-BODIPY and MXene (see Scheme 1). The as-prepared functionalized MXene (BODIPY-MXene) was introduced into ABS resin to prepare nanocomposites. The thermal stability, mechanical and flammability properties of the ABS nanocomposites were evaluated. The heat release and toxicity emissions in burning were emphatically studied by means of cone calorimeter coupled with FTIR, and the underlying mechanisms that led to flammability and smoke reductions were discussed.

2. Experimental

2.1. Raw materials

ABS resin (AG15A1) was supplied by Taiwan Petrochemical Industry. MAX (Ti_3AlC_2) was provided by the 11 Nano Technology Co., Ltd., (Changchun, China). N, N'-dimethylformamide (DMF, AR), dichloromethane (AR), ethanol (AR), tetrahydrofuran (THF, AR), acetone (AR), *p*-nitrobenzaldehyde (AR), 2, 4-dimethylpyrrole (AR), petroleum ether (AR), triethylamine (AR), boron trifluoride diethyl etherate (AR), anhydrous sodium sulfate (AR), hydrochloric acid (HCl, 36.0–38.0 aq.) were purchased from the Sinopharm Chemical Reagent Co. Ltd. (Shanghai, China). Lithium fluoride (LiF, AR, 99%) was supplied from the Aladdin Reagent Co. Ltd., China. All chemicals were used without further purification.

2.2. Synthesis of BODIPY

BODIPY containing amino group was synthesized via the reaction between 2, 4-dimethylpyrrole and *p*-nitrobenzaldehyde followed by the reduction of the nitro group [42]. The detailed procedure was described in the Supplementary Material.

2.3. Preparation of BODIPY-MXene nanosheets

Before interface decoration, MAX (Ti_3AlC_2) was etched in the mixture of concentrated HCl (9 M) and LiF followed by the ultrasonic treatment in deionized (DI) water for preparing exfoliated MXene ($Ti_3C_2T_x$) nanosheets, as detailed in our previous work [36–38]. Amino-BODIPY dissolved in ethanol was protonated to form $-NH_3^+$ using HCl aqueous solution (0.1 M) until pH = 1, named as BODIPY-NH_3^+ BODIPY-MXene nanosheets were fabricated by electrostatic interactions between negative MXene and protonated positive-charge BODIPY, as illustrated in Scheme 1. Typically, BODIPY-NH_3^+ dissolved in ethanol (1 mg/mL) was added slowly into the MXene suspension (1 mg/mL) at BODIPY/MXene weight ratio of 1/1 with continuous stirring for 1 h.

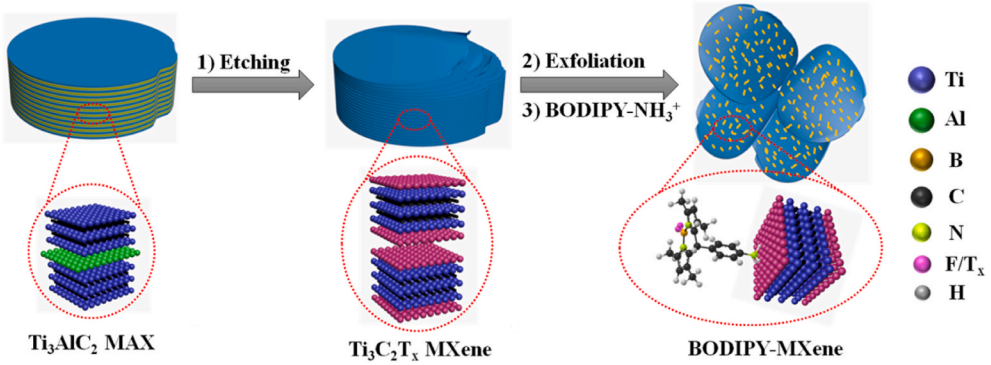

Scheme 1. Schematic preparation route of BODIPY-MXene nanosheets.

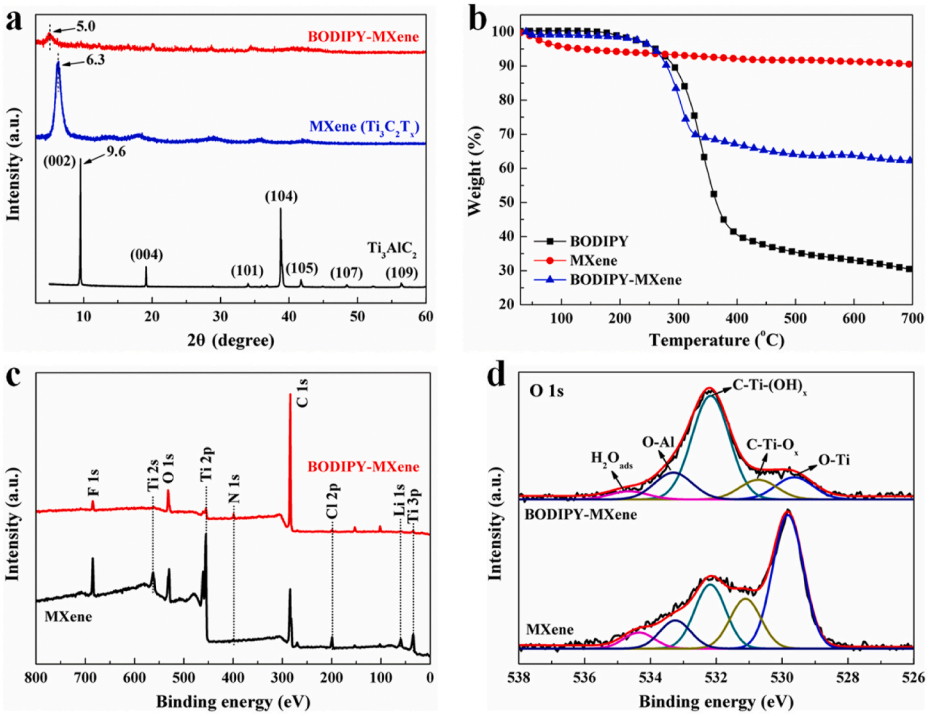

Fig. 1. XRD patterns (a) and TGA curves (b) of Ti_3AlC_2, MXene and BODIPY-MXene; (c) XPS spectra of MXene and BODIPY-MXene; (d) high resolution O 1s spectra of MXene and BODIPY-MXene.

After the reaction, dark green BODIPY-MXene precipitates were collected by centrifugation followed by washing with ethanol and DI water, and subsequently freeze-drying procedures.

2.4. Fabrication of ABS/BODIPY-MXene nanocomposites

ABS/BODIPY-MXene nanocomposites were prepared via a co-coagulation method followed by compression molding according to a similar procedure reported in our previous work [36–38]. To manufacture the ABS nanocomposites filled with 0.5 wt% of BODIPY-MXene, BODIPY-MXene (0.1 g) was dispersed in 100 mL of THF with sonication assistance (45 min) to attain a uniform dispersion. ABS (19.9 g) was subsequently added into the BODIPY-MXene dispersion with mechanical stirring until complete dissolution of the ABS. Finally, the ABS/BODIPY-MXene suspension was poured into DI water followed by washing with ethanol. The ABS/BODIPY-MXene floccules were collected and dried at 60 °C for 12 h in a vacuum oven to remove the residual solvent. All the ABS samples with standard sizes were prepared via hot press. In this work, ABS/BODIPY-MXene0.5 and ABS/BODIPY-MXene2.0 respectively represent the ABS nanocomposites with 0.5 and 2.0 wt% concentration of BODIPY-MXene. For comparison, ABS/BODIPY2.0 containing 2.0 wt% of BODIPY was prepared according to the same procedure.

2.5. Characterizations and measurements

The chemical structure of BODIPY-NO_2 and BODIPY-NH_2 was characterized by ^{1}H NMR spectra recorded on a 400 MHz AVANCE III Bruker NMR spectrometer, using deuterated chloroform ($CDCl_3$) as the solvent and tetramethysilane (TMS) as an internal standard.

X-ray diffraction (XRD) was conducted on an X-ray diffractometer (Rigaku Co., Japan) with a Cu Kα radiation (λ = 0.1542 nm).

Thermogravimetric analysis (TGA) was conducted using a TGA Q5000IR thermo-analyzer (TA Instruments Inc., USA) at a heating rate of 20 °C/min under nitrogen/air condition. 5–10 mg specimen was used to characterize the thermal/thermal-oxidation decomposition behaviors of neat ABS and ABS composites. Each sample was repeated for three times.

X-ray photoelectron spectroscopy (XPS) was utilized to study the surface chemical composition of samples using a VG Escalab Mark II spectrometer equipped with an Al Kα excitation radiation (hυ = 1486.6 eV).

Scanning electron microscope (SEM) was conducted on a Hitachi SU8200 SEM (Tokyo, Japan) with the acceleration voltage of 10 kV. Sample powders were coated on the surface of conductive tapes, followed by the deposition of gold on the surface of samples by magnetron sputtering.

Transmission electron microscopy (TEM) was employed to observe the morphology of samples using a JEOL JEM-2100 instrument (Tokyo, Japan) with an acceleration voltage of 200 kV. Prior to observation, the nanocomposite specimens were cut into ultrathin slices under cryogenic conditions with an ultramicrotome (Ultraacut-1, U K) equipped with a diamond knife.

The tensile properties of neat ABS and ABS composites were determined by using a Universal Mechanical Testing Machine (YF-900, Yuanfeng testing equipment Co., Ltd, Yangzhou, China). The crosshead speed was 50 mm/min for tensile properties. An average of five individual determinations was gained.

Limiting oxygen index (LOI) of neat ABS and ABS composites was evaluated by means of an HC-2 Oxygen Index instrument (Jiangning Analytical Instrument Co. Ltd., Nanjing, China) according to ASTM D2863-2008. The sample size in the test was 100 × 6.5 × 3 mm^3.

Cone calorimeter coupled with FTIR (iCone Classic, Fire Testing Technology, UK) was employed to evaluate the burning behavior and toxicity hazards of neat ABS and ABS composites at an incident flux of 35 kW/m^2. Prior to tests, all the samples with the dimensions of 100 × 100 × 3 mm^3 were wrapped with aluminium foil. Each sample was repeated for three times.

The residues collected in cone calorimeter tests were analyzed by using a SU8010 field-emission SEM (FESEM, Japan) at an acceleration voltage of 10 kV, XRD (Rigaku Co., Japan) and Raman spectra in the wavenumber range of 500–2000 cm^{-1} (Laser confocal micro Raman

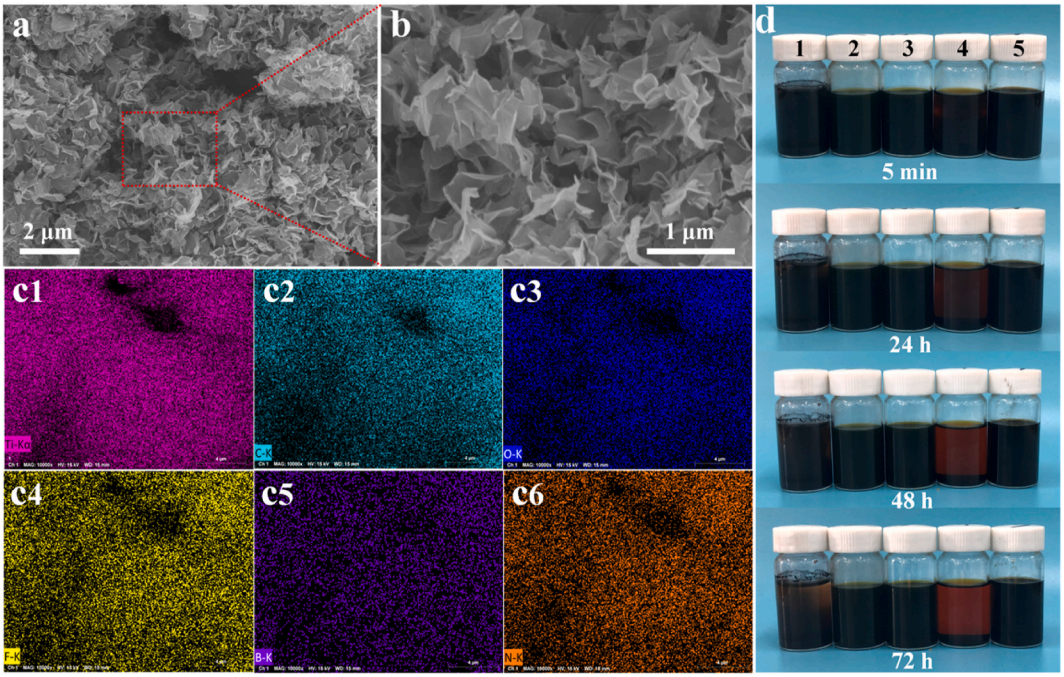

Fig. 2. SEM images of BODIPY-MXene (a, b) and elemental mapping (c1-c6); (d) Dispersion of BODIPY-MXene in various solvents for a period of time: 1-water, 2-CH_2Cl_2, 3-THF, 4-ethanol, 5-DMF.

spectrometer of Thermo Fisher, DXR, USA).

3. Results and discussion

3.1. Structure, morphology and dispersion of BODIPY-MXene

Fig. 1a shows the XRD patterns of Ti_3AlC_2, MXene ($Ti_3C_2T_x$) and BODIPY-MXene. Compared with Ti_3AlC_2, MXene ($Ti_3C_2T_x$) exhibits a completely different structure. The (002) diffraction peak of Ti_3AlC_2 shifts from 9.5° to 6.3°, and the corresponding interlayer distance increases from 0.93 to 1.40 nm. The (104) diffraction peak of Ti_3AlC_2 at 38.8° is attributed to Al layer. There are almost no diffraction peaks at 35–40° in MXene, indicating that the Al layer in Ti_3AlC_2 has been successfully etched. After modification by BODIPY, the (002) diffraction peak of MXene moves from 6.3° to 5.0° corresponding to the increase in interlayer distance from 1.40 to 1.77 nm. This shift indicates that the BODIPY is attached to the surface of MXene nanosheets, which further expands the interlayer distance. Simultaneously, compared with MXene, the intensity of the (002) diffraction peak for BODIPY-MXene is significantly reduced, indicating that the highly ordered arrangement of MXene nanosheets is disrupted by the introduction of BODIPY, resulting in the decrease of crystallinity.

Fig. 1b exhibits the TGA curves of BODIPY, MXene and BODIPY-MXene under nitrogen condition. BODIPY decomposes at 260 °C (the temperature at 5% weight loss, $T_{-5\%}$) with 30.5 wt% residues at 700 °C, which is attributed to the thermal decomposition of organics. MXene starts the decomposition at 135 °C ($T_{-5\%}$). At 700 °C, the residual amount is 90.6 wt% corresponding to the removal of adsorbed water and the decomposition of organic functional groups (i.e. OH, O, F). The thermal decomposition temperature of BODIPY-MXene is obviously higher than that of MXene. It begins to decompose at 260 °C. The residual amount at 700 °C is 62.2 wt% that is ascribed to the decomposition of BODIPY and functional groups on MXene. In the interface decoration reaction, the mass ratio of BODIPY and MXene is 1:1. According to the complete reaction calculation, the overall weight loss should be 39.5 wt%, whereas the actual weight loss is 37.8 wt%. The experimental weight loss is lower than calculated value, indicating that all the BODIPY molecules are grafted on the MXene nanosheets. The improved char residues amount implies the interaction between MXene and BODIPY. It is probably attributed to the carbonization of BODIPY catalyzed by MXene leading to the increased volume of char residues.

XPS analysis (Fig. 1c) exhibits that Al layer is etched from Ti_3AlC_2 to generate $Ti_3C_2T_x$ (MXene) with traces of Li 1s, Cl 2p and F 1s at 59.5, 199.2 and 684.5 eV, respectively. The introduction of BODIPY to MXene leads to the increasing intensity of C element. The C/Ti atomic ratio in BODIPY-MXene is approximately 29.7, much higher than that in MXene (2.7) (see Table S2). Additionally, the peaks corresponding to Ti 3p, Ti 2s and Cl 2p almost disappear in the spectrum of BODIPY-MXene. It suggests that numerous BODIPY molecules are well coated on the surface of MXene nanosheets. As a result, the concentration of C element sharply increases, and the characteristic elements (Ti 3p, Ti 2s and Cl 2p) are hardly detected. The peak at 399.5 eV (N 1s) can be observed in BODIPY-MXene, which further confirms the decoration of BODIPY on MXene nanosheets. In O 1s spectra (Fig. 1d), the peaks at ~529.8, 531.1, 532.2, 533.3 and 534.4 eV are ascribed to O–Ti (TiO_2), C–Ti-O_x (I), C–Ti-$(OH)_x$ (II), O–Al (Al_2O_3) and H_2O_{ads} bonds, respectively [43–45]. The atomic percentage of C–Ti-$(OH)_x$ in all fitted components increases from 30.0% for MXene to 57.5% for BODIPY-MXene, indicating the strong interaction between BODIPY and MXene layers (see Table S3). In addition, the atomic percentage of O–Ti (TiO_2) is reduced from 45.8% for MXene to 12.3% for BODIPY-MXene, suggesting that the oxidation of MXene is significantly suppressed.

SEM images of BODIPY-MXene at various magnifications are shown in Fig. 2 (a, b) and Fig. S5. The exfoliated MXene ($Ti_3C_2T_x$) nanosheets possess a hexagonal crystalline structure with the lateral size distribution ranged from 0.1 to 1.3 μm, concentrating at approximately 0.3–0.5 μm, and ultrathin thickness (around 2 nm), which has been characterized in our previous studies [36,46–48]. After etching and exfoliation, there are many negative charges on the surface of as-prepared MXene ($Ti_3C_2T_x$) nanosheets. The BODIPY cationic modifiers play a role in controlling the size, shape and surface polarity of the negative nanosheets [36–38]. As illustrated in Fig. 2 (a, b) and Fig. S5, BODIPY-MXene clearly exhibits graphene-like nanosheets with ripples. They are stacked with fluffy morphology rather than aggregation, which is beneficial for

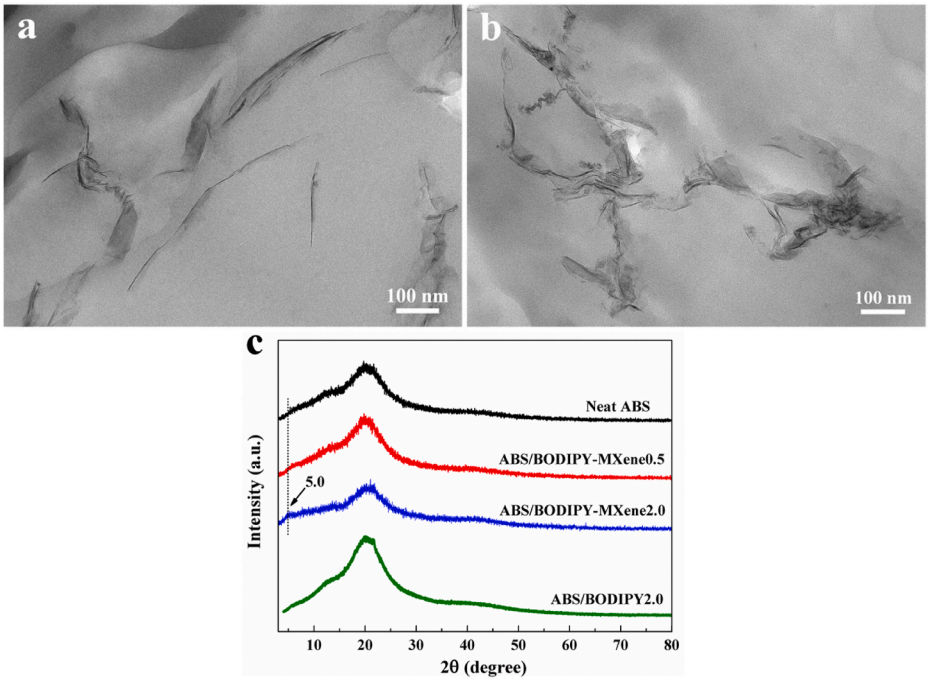

Fig. 3. TEM images of ABS/BODIPY-MXene0.5 (a) and ABS/BODIPY-MXene2.0 (b); XRD patterns (c) neat ABS and ABS composites.

the dispersion in organic solvents or polymers. Fig. 2 (c1-c6) shows the element mapping of BODIPY-MXene nanosheets. It is observed that all the elements, Ti, C, O, F, B and N, are uniformly distributed in the coverage of Fig. 2a. B and N are the characteristic elements of BODIPY, indicating the grafted BODIPY on MXene nanosheets.

To evaluate the dispersion of BODIPY-MXene in common solvents, BODIPY-MXene was dispersed in five solvents for a fixed period of time, including water, CH_2Cl_2, THF, ethanol and DMF (see Fig. 2d). BODIPY-MXene exhibits poor dispersion in polar solvents (i.e. water and ethanol), which is evidenced by the apparent sediment at the bottom of the bottle after standing for 24–48 h. This is because the introduction of BODIPY promotes a change in the surface property of MXene nanosheets from hydrophilic to hydrophobic. As expected, BODIPY-MXene nanosheets are steadily dispersed in CH_2Cl_2, THF and DMF for 72 h. After 96 h, the precipitation in CH_2Cl_2 can be observed, while the uniform dispersion in THF and DMF can be maintained for 168 h or longer (see Fig. S6). The phenomenon indicates that it is more suitable for BODIPY-MXene to be dispersed in low-polar solvents facilitating the fabrication of polymer nanocomposites via solvent blending and dispersion of BODIPY-MXene in polymer matrix.

3.2. Morphology and structure of ABS composites

The morphology and structure of ABS/BODIPY-MXene composites were evaluated by TEM and XRD. As illustrated in Fig. 3a and Fig. S7a, BODIPY-MXene nanosheets with a low loading can be homogeneously dispersed in ABS. There is no obvious aggregation. Furthermore, it is observed that single-/few-layer MXene nano-flakes are distributed in the ABS matrix, suggesting the good dispersion. However, when the concentration of BODIPY-MXene increases to 2.0 wt%, the aggregation appears (see Fig. 3b and Fig. S7b). Fig. 3c shows the XRD patterns of neat ABS and ABS composites, in which the broad peaks at around 20° for all samples are observed, indicating that ABS resin is amorphous in nature [49]. The weak peak at 5.0° in ABS/BODIPY-MXene2.0 is attributed to the (002) diffraction of BODIPY-MXene (see Fig. 1a). The unchanged 2θ suggests that the ABS macromolecules can not enter into the interlayers of BODIPY-MXene nanosheets to expand the interlayer distance. As a result, the nanoparticles aggregation for ABS/BODIPY-MXene2.0 is more significant compared to ABS/BODIPY-MXene0.5.

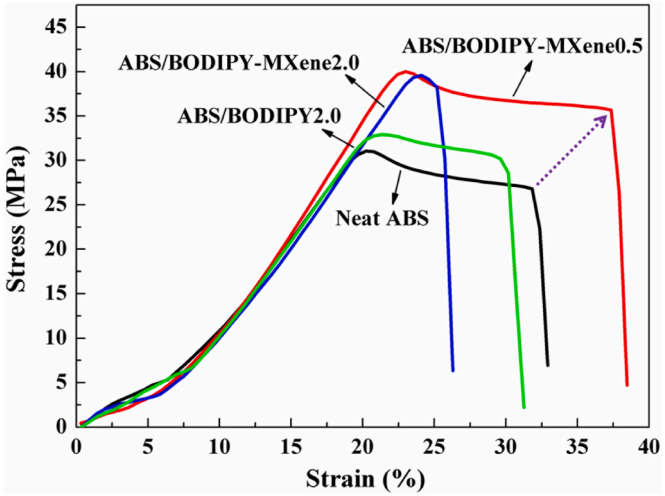

Fig. 4. Stress-strain curves of neat ABS and ABS composites.

Table 2
Tensile properties of neat ABS and ABS composies.

Sample	Tensile strengh (MPa)	Young's modulus (MPa)	Elongation at break (%)
Neat ABS	31.3 ± 5.2	2223 ± 248	33.5 ± 5.0
ABS/BODIPY-MXene0.5	40.0 ± 1.4	2636 ± 225	39.5 ± 9.5
ABS/BODIPY-MXene2.0	38.4 ± 3.7	2770 ± 212	28.5 ± 2.2
ABS/BODIPY2.0	31.9 ± 4.9	2277 ± 359	37.4 ± 6.2

3.3. Tensile properties of ABS composites

Fig. 4 shows the stress-strain curves for pure ABS and ABS

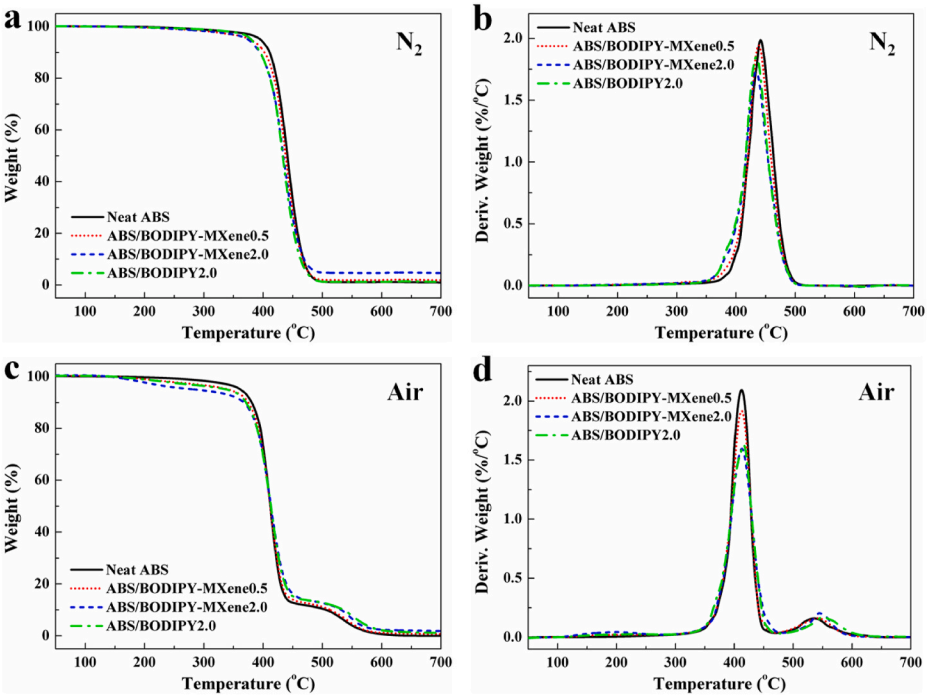

Fig. 5. TG (a, c) and DTG (b, d) curves of neat ABS and ABS composites under N_2 and air condition.

Table 3
TGA data of neat ABS and ABS composies. (20 °C/min, 5–10 mg; error: ± 1 °C, ± 0.2 wt%; 25–700 °C).

Sample	Nitrogen atmosphere				Air atmosphere			
	$T_{-5\%}$ (°C)	T_{max} (°C)	MLR_{max} (wt%/°C)	Res [a] (wt%)	$T_{-5\%}$ (°C)	T_{max1}/T_{max2} (°C)	MLR_{max} (wt%/°C)	Res (wt%)
Neat ABS	399	442	2.0	1.0	362	412/535	2.1	0.1
ABS/BODIPY-MXene0.5	384	438	1.9	1.9	343	412/542	1.9	0.7
ABS/BODIPY-MXene2.0	379	434	1.7	4.7	286	413/545	1.6	1.9
ABS/BODIPY2.0	383	434	1.8	1.2	339	416/551	1.6	1.1

[a] Res: Residues at 700 °C (wt%).

composites. The related data are listed in Table 2. The addition of BODIPY into ABS has no fundamental influence on tensile strength, Young's modulus and elongation at break. On the contrary, the introduction of BODIPY-MXene can efficiently improve the tensile strength and modulus of ABS. For example, the tensile strength and Young's modulus increase from 31.3 MPa and 2223 MPa for neat ABS to 40.0 MPa and 2636 MPa for ABS/BODIPY-MXene0.5 with the improvement of 27.8% and 18.6% respectively. In addition, the elongation at break for ABS/BODIPY-MXene0.5 is increased by 17.9% compared to the control ABS. It suggests that a low loading of BODIPY-MXene can enhance the mechanical strength and toughness of ABS via the excellent dispersion and strong interfacial adhesion between BODIPY-MXene and ABS chains that allow for a large deformation to maintain integrality [50]. When the nano-additive loading increases to 2.0 wt%, the elongation at break is dramatically reduced despite the improved tensile strength and modulus (see Fig. 4 and Table 2). From Fig. 3b and Fig. S7b, it can be observed that the loading of BODIPY-MXene nanosheets at 2.0 wt% in ABS tend to aggregation leading to the reduction of interfacial interaction between BODIPY-MXene and ABS. Accordingly, micro-voids may occur at the interface resulting from the reduced interfacial adhesion that can destroy the continuous structure of ABS. On the other hand, the aggregation restricts the mobility of ABS molecular chains more significantly compared to ABS/BODIPY-MXene0.5. Therefore, the toughness of ABS/BODIPY-MXene2.0 is reduced.

3.4. Thermal decomposition behaviors of ABS composites

The thermal decomposition behaviors of neat ABS and ABS composites under nitrogen condition are illustrated in Fig. 5 (a, b), and the related data are summarized in Table 3. ABS, a copolymer composed of three components, undergoes a one-stage decomposition that produces large amounts of flammable aromatic and aliphatic hydrocarbons and toxic gases (i.e. HCN, NH_3) [51]. ABS starts to decompose at 399 °C ($T_{-5\%}$) with a maximum decomposition rate at 442 °C and negligible char residues at about 500 °C [51]. It indicates that the carbonization of ABS is very difficult. Both the addition of BODIPY and BODIPY-MXene reduce the onset decomposition temperature due to the early degradation of BODIPY and surface termination groups (i.e. F, O, OH). The 0.5 wt% loading of BODIPY-MXene has the lowest influence on the thermal stability of ABS (see Table 3). Fortunately, the presence of BODIPY-MXene promotes the char formation of ABS composites and the effect increases with the loading (2.0 wt%) compared to BODIPY. For example, the theoretical char yield of ABS/BODIPY-MXene2.0 is calculated at around 2.2 wt% based on the char yields of BODIPY-MXene (62.2 wt%) and ABS (1.0 wt%) at 700 °C under nitrogen condition, while the sample has a higher experimental char yield of 4.7 wt%. Conversely, the theoretical char yield of ABS/BODIPY2.0 is approximatively 1.6 wt%, and the experimental char yield is 1.2 wt%. It indicates that the introduction of BODIPY-MXene can promote the carbonization of ABS. In addition, ABS/BODIPY-MXene2.0 records the lowest peak of mass loss rate (MLR_{max}) compared to all the other

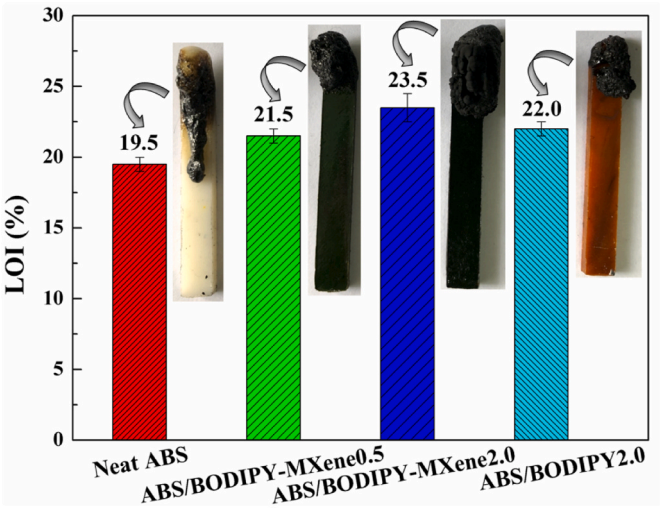

Fig. 6. LOI testing results and embedded digital photos of neat ABS and ABS composites.

composites (Fig. 5b and Table 3), further confirming the enhanced char formation effect of BODIPY-MXene which will increase the thermal protection of the underlying matrix against fire.

The thermal-oxidation decomposition behaviors of neat ABS and ABS composites in air atmosphere are exhibited in Fig. 5 (c, d), and the related data are listed in Table 3. The thermo-oxidative decomposition of ABS is more complicated due to the two-step degradation [52]. The first step occurs from 362 to 448 °C with a weight loss of 82 wt% for neat ABS. The second step ranges from 495 to 610 °C with only 0.4 wt% residues left indicating the complete degradation. Both the addition of BODIPY and BODIPY-MXene cause the earlier thermal-oxidation decomposition owing to the lower thermal stability of BODIPY and BODIPY-MXene compared to ABS. ABS/BODIPY-MXene2.0 shows the lowest initial decomposition temperature (286 °C). It is probably attributed to the ease of oxidation and degradation of BODIPY-MXene inducing the formation of various polymer radicals that accelerate the degradation of ABS chains [53] (Fig. S8). After the first decomposition step, the ABS composites exhibit obviously improved char residues compared to neat ABS. The char residues at 460 °C are 12.3 wt%, 13.2 wt%, 14.8 wt% and 14.1 wt% for neat ABS, ABS/BODIPY-MXene0.5, ABS/BODIPY-MXene2.0 and ABS/BODIPY2.0. Combined with the thermal-oxidation degradation of BODIPY and BODIPY-MXene (see Fig. S8), BODIPY-MXene shows more significant charring effect on ABS resin than BODIPY. In the second decomposition step, the higher T_{max2} values for ABS composites indicate that the char residues generated in the first step inhibit the degradation of ABS fragments. Moreover, the lowest MLR_{max} for ABS/BODIPY-MXene2.0 (1.6 wt%/°C) further confirms the charring effect of BODIPY-MXene in comparison with pure ABS

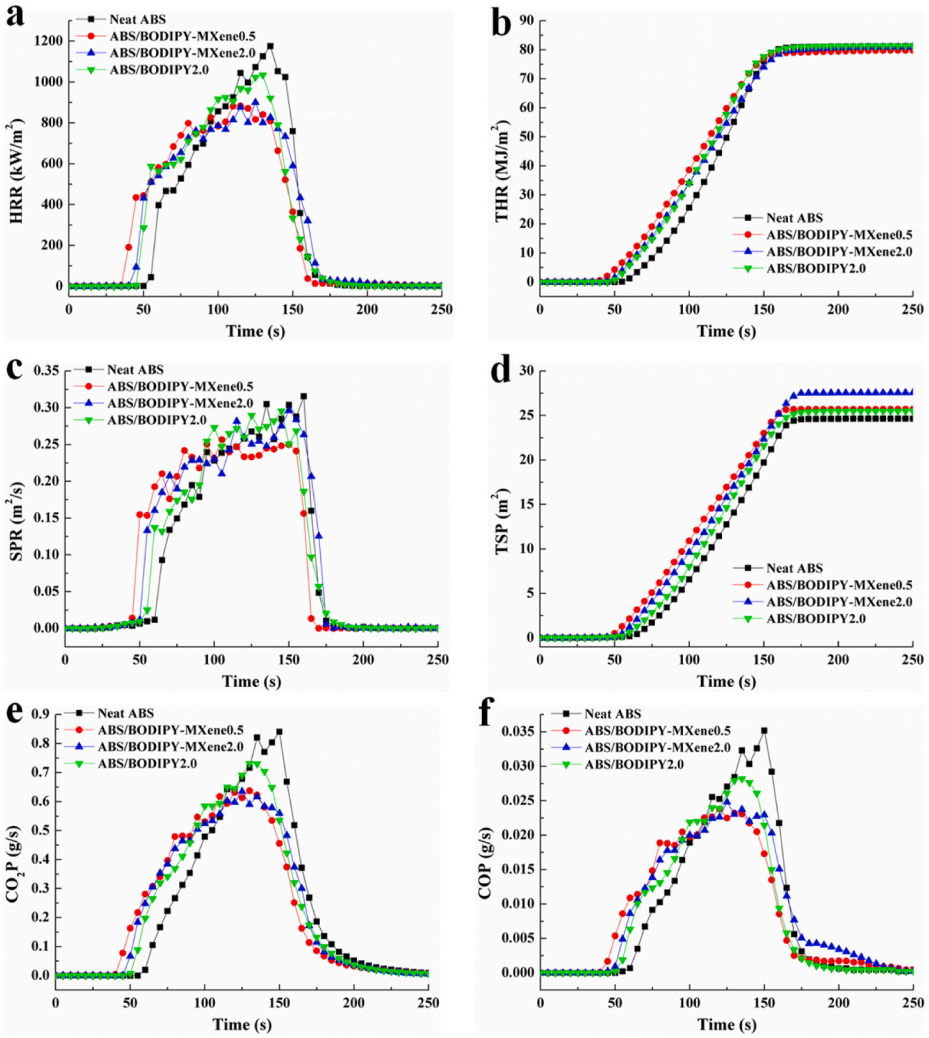

Fig. 7. HRR (a), THR (b), SPR (c), TSP (d), CO_2 (e) and CO (f) production as a function of the burning time for ABS and its composites.

Table 4
Cone calorimeter data of ABS and its composites at 35 kW/m^2 (TTI: time to ignition; PHRR: peak heat release rate; THR: total heat release; PSPR: peak smoke production rate; TSP: total smoke production; PCOP: peak CO production; PCO_2P: peak CO_2 production.)

Sample	TTI (s)	PHRR (kW/m^2)	THR (MJ/m^2)	PSPR (m^2/s)	TSP (m^2)	PCOP (g/s)	PCO_2P (g/s)
Error	±2	±15	±0.5	±0.01	±0.5	±0.005	±0.02
Neat ABS	51	1174	81.2	0.315	24.7	0.035	0.84
ABS/BODIPY-MXene0.5	35	886	79.8	0.257	25.7	0.023	0.64
ABS/BODIPY-MXene2.0	40	900	81.0	0.296	27.6	0.025	0.64
ABS/BODIPY2.0	45	1032	81.3	0.296	25.6	0.028	0.73

(2.1 wt%/°C).

3.5. Fire safety performance of ABS composites

LOI is one of the most commonly used benchmark measurements for evaluating the burning behaviors of polymeric materials. Fig. 6 shows the LOI results for neat ABS and ABS composites. ABS is a flammable plastic with a LOI of 19.5%. In the burning of pure ABS, there is an obvious molten droplet that continuously flows downward along the specimen leading to the acceleration of combustion (Fig. 6). Interestingly, both the introduction of BODIPY and BODIPY-MXene restrain the dripping of ABS through rapid carbonization even at the low loading of 0.5 wt% BODIPY-MXene, which is in good agreement with the thermal decomposition behaviors under air condition (see Fig. 5 and Table 3). Furthermore, ABS/BODIPY-MXene2.0 shows more remarkable charring effect than the other composites resulting in the enhancement of LOI (23.5%). In consideration of the low concentration (0.5 and 2.0 wt%), the improved LOI values (+2% and +4%) respectively for ABS/BODIPY-MXene0.5 and ABS/BODIPY-MXene2.0 imply that the flame retardancy of BODIPY-MXene for ABS is more effective than that of BODIPY (increased by 2.5% at 2.0 wt%).

Cone calorimeter coupled with FTIR was utilized to measure the flammability, smoke and toxic fumes of ABS and its composites. The results are shown in Fig. 7 and Table 4. The control ABS is ignited at around 51 s (time to ignition, TTI), and has the highest heat release rate with a peak heat release rate (PHRR) of 1174 kW/m^2, which is regarded as a highly flammable polymer. The loading of all the additives reduces the TTI values, which may be attributed to the early degradation of BODIPY and BODIPY-MXene and the endothermic effect of dark green BODIPY-MXene causing heat accumulation on the specimen surface [38]. The introduction of 2.0 wt% BODIPY to ABS leads to the slight reduction of PHRR (reduced by 12.0%), which is attributed to the free radical capture by halides decomposed from BODIPY. In the thermal oxidative degradation of BODIPY, the volatiles, including HF, CO_2, H_2O and N_2 are released, leaving B_2O_3 solids [54]. HF plays the dominant role of scavenging free radicals in a gas phase which is similar to

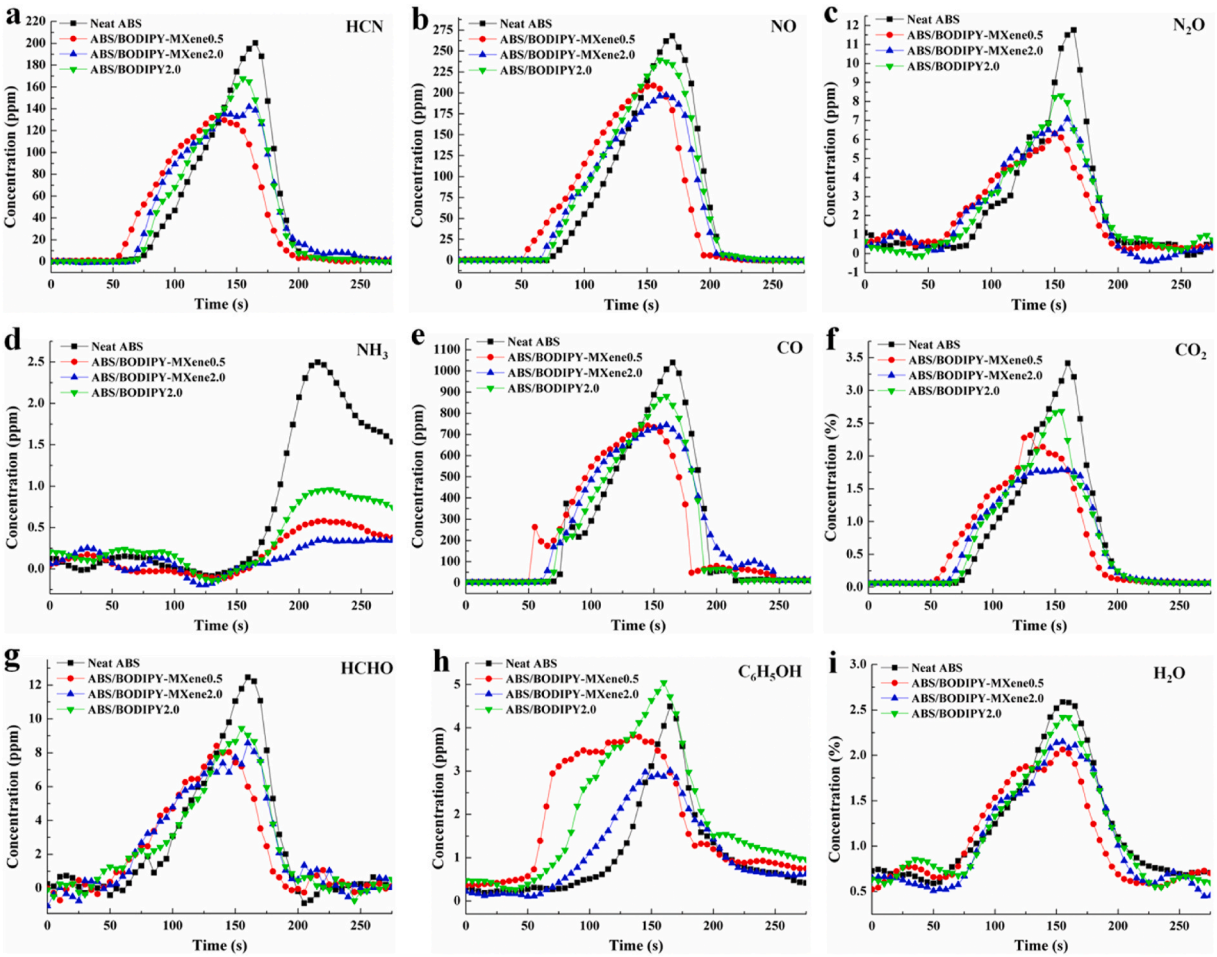

Fig. 8. FTIR gas analysis of ABS and its composites.

Table 5
FTIR data-Peak concentration of gases releases.

Sample	HCN (ppm)	NO (ppm)	N_2O (ppm)	NH_3 (ppm)	CO (ppm)	CO_2 (%)	HCHO (ppm)	C_6H_5OH (ppm)	H_2O (%)	C_2H_4 (ppm)
Error	±5	±5	±0.5	±0.1	±10	±0.1	±0.1	±0.1	±0.1	±0.5
Neat ABS	200	268	11.8	2.5	1041	3.4	12.5	4.5	2.6	34.0
ABS/BODIPY-MXene0.5	133	209	6.3	0.6	741	2.3	8.4	3.8	2.1	22.2
ABS/BODIPY-MXene2.0	142	198	7.1	0.4	747	1.8	8.6	3.0	2.2	24.3
ABS/BODIPY2.0	167	239	8.3	1.0	877	2.7	9.5	5.0	2.4	25.1

Table 6
FTIR data-Quantification of gases releases.

Sample	HCN (ppm)	NO (ppm)	N_2O (ppm)	NH_3 (ppm)	CO (ppm)	CO_2 (%)	HCHO (ppm)	C_6H_5OH (ppm)	H_2O (%)	C_2H_4 (ppm)
Error	±500	±500	±50	±20	±500	±20	±50	±50	±20	±100
Neat ABS	12,410	18,002	690	243	72,687	214	762	323	356	2253
ABS/BODIPY-MXene0.5	11,508	17,460	574	55	69,385	192	645	522	304	2014
ABS/BODIPY-MXene 2.0	12,434	16,756	599	43	74,293	182	733	327	306	2223
ABS/BODIPY2.0	12,079	18,861	672	149	69,114	198	682	586	361	2074

chlorinated and brominated flame retardants [55]. Compared to the control ABS, the PHRR reduces from 1174 kW/m^2 to 886 kW/m^2 for ABS/BODIPY-MXene0.5 with a reduction of 24.5%. In addition, the incorporation of BODIPY-MXene can also inhibit the release of smoke and CO, CO_2. As shown in Fig. 7 (c, e, f) and Table 4, the reduction of peak smoke production rate (PSPR), peak CO production (PCOP) and PCO_2P for ABS/BODIPY-MXene0.5 is 18.4%, 34.3% and 23.8% respectively, compared to the control ABS. However, increasing the loading of BODIPY-MXene cannot lead to the further reduction in heat release, smoke, CO, and CO_2 productions. On the contrary, ABS/BODIPY-MXene2.0 shows the highest TSP. There are two primary reasons: 1) the aggregation of BODIPY-MXene nanosheets results in the limited flame retardant effect; 2) the introduction of numerous HF inhibitors into the flame remarkably reduces the concentration of hydrogen, hydroxide, and hydrocarbon radicals leading to the increase of the C_2 diradicals and soot [55]. The flame retardant mechanism will be discussed in depth later .

The evaluation of toxic and asphyxiant gases generated during polymer combustion is vital to the assessment of fire hazards in compartment or wildland fire scenarios [4,36,56]. Taking advantages of FTIR real-time monitoring in the combustion, various toxicity volatiles, including HCN, NO, N_2O, NH_3, CO, CO_2, formaldehyde (HCHO) and phenol (C_6H_5OH), have been detected, as shown in Fig. 8 and Table 5. As expected, these curves follow a similar shape with HRR curves in the cone calorimeter tests except NH_3. The control ABS records higher peak concentration of toxic and asphyxiant gases compared to its composites. With the introduction of 2.0 wt% BODIPY, the reductions of peak concentration for HCN, NO, N_2O, CO and CO_2 are not remarkable, suggesting that the smoke suppression of BODIPY is very limited. For comparison, the loading of 0.5 wt% BODIPY-MXene into ABS leads to the reduced peak concentration of HCN (−33.5%), NO (−22.0%), N_2O (−46.6%), NH_3 (−76.0%), CO (−28.8%), CO_2 (−32.4%), HCHO (−32.8%) and C_6H_5OH (−15.6%), which is probably attributed to the better dispersion of BODIPY-MXene nanosheets in ABS contributing to the catalytic flame retardant effect. ABS/BODIPY-MXene2.0 shows the lower peak concentration for NH_3 (−84.0%), CO_2 (−47.1%) and C_6H_5OH (−33.3%) compared to ABS/BODIPY-MXene0.5 and ABS/BODIPY2.0, indicating the synergistic inhibition effect between BODIPY and MXene.

To further evaluate the toxicity hazards, the volatiles were quantified based on the integral area of toxic gases yield curves in Fig. 8 [4], which are listed in Table 6. It is observed that both the addition of BODIPY and BODIPY-MXene can not dramatically reduce the total amounts of these gases, which are in agreement with the THR trends (see Fig. 7b). Interestingly, ABS/BODIPY-MXene2.0 shows more significant reduction of the total amounts of NO (−7.0%), N_2O (−13.2%) and NH_3 (−82.3%) compared to ABS/BODIPY2.0. These results indicate that the loading of BODIPY-MXene to ABS leads to a change in combustion reaction chemistry as well as the reduction of toxic gases containing nitrogen. We planned to compare ABS composites with other reported results to benchmark the remarkable progress in toxicity hazards reductions. Unfortunately, the related studies were very limited. Prieur et al. [4] reported that the addition of 30 wt% phosphorylated lignin (P-LIG) into ABS reduced the peak concentration of HCN (−27%), NO (−47%), CO (−30%), CO_2 (−47%). Despite the suppression effect on toxic gases, the wt% loading of P-LIG is much higher than that of BODIPY-MXene in this work. Consequently, it can be concluded that the toxicity reduction by BODIPY-MXene is highly efficient.

3.6. Flame retardant mechanism

The flame retardant mechanism of ABS composites can be clarified on the basis of gas- and condensed-phase analysis. In gas-phase, the release of CO, CO_2 and H_2O is the indicator of the combustion. As shown in Fig. 8 (e, f, i), the inhibition on CO, CO_2 and H_2O by BODIPY-MXene is more significant than BODIPY. Additionally, the CO/CO_2 ratios in total amount for ABS/BODIPY-MXene0.5 and ABS/BODIPY-MXene2.0 are 0.036 and 0.041 respectively, which are higher than that for control ABS (0.034) and ABS/BODIPY2.0 (0.035), suggesting the higher incomplete combustion of ABS/BODIPY-MXene nanocomposites. Ethylene (C_2H_4) is a flammable fuel decomposed from ABS that is another indicator of the combustion. As illustrated in Fig. S9, the broad and lower peaks for ABS/BODIPY-MXene nanocomposites confirm the reduced PHRR. Despite the decreased peak concentration of ethylene, the total amount is unchanged. It indicates that the addition of BODIPY-MXene prolongs the burning of ABS composites leading to the reduction of PHRR while most of the decomposed products are burnt. On the other hand, the higher degree of incomplete combustion for ABS/BODIPY-MXene2.0 suggests more soot production. The higher TSP value for ABS/BODIPY-MXene2.0 can support this assumption (see Fig. 7d and Table 4). The formation of carbon particles is attributed to the free radicals trapping effect caused by BODIPY-MXene. In the decomposition of BODIPY-MXene, a large number of fluorine atoms are released to the gas phase. Simultaneously, the barrier and catalytic effect contributed by MXene nanosheets prolong the residence of fluorine atoms in the flame zone so that more “hot” radicals derived from ABS are scavenged [55]. In the combustion of ABS composites, the traces of HF are detected as shown in Fig. S10. It indicates that F atom and HF are involved in the radical reaction, which promotes the incomplete combustion, leading to more soot formation.

The carbonization of ABS is very difficult due to its extremely rapid degradation under elevated temperatures. To evaluate the condensed phase, the char residues for ABS/BODIPY2.0, ABS/BODIPY-MXene0.5

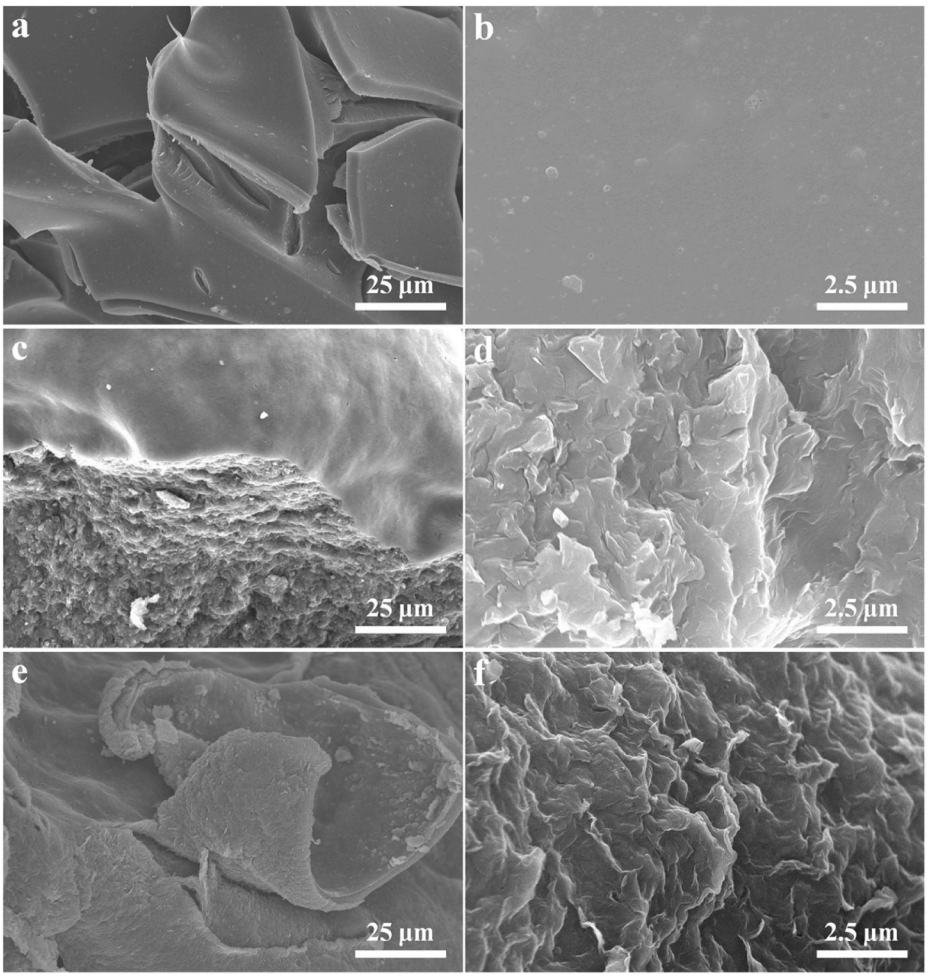

Fig. 9. SEM images of the corresponding residues for ABS/BODIPY2.0 (a, b), ABS/BODIPY-MXene0.5 (c, d) and ABS/BODIPY-MXene2.0 (e, f) after LOI tests.

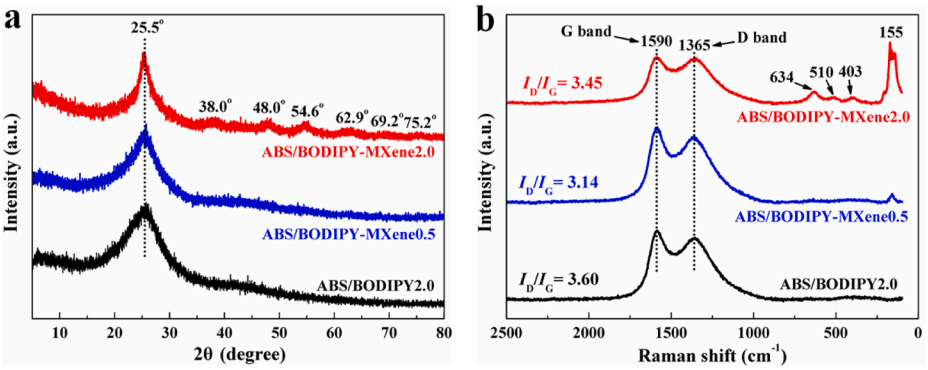

Fig. 10. XRD patterns (a) and Raman spectra (b) of the char residues for ABS composites.

and ABS/BODIPY-MXene2.0 after LOI tests were studied with SEM, XRD and Raman spectra. ABS/BODIPY2.0 shows a solid char morphology with cracks (Fig. 9a). In higher magnification (Fig. 9b), there are some tiny pores distributed on the char surface. The obvious cracks and pores indicate that the inhibition on the emission of flammable decomposed products is limited during the combustion of ABS/BODIPY2.0, which is consistent with LOI and cone calorimeter testing results. For ABS/BODIPY-MXene0.5, tightly stacked char layers can be clearly found in the cross-section of residues (Fig. 9c). The higher magnified SEM image (Fig. 9d) shows the compact char residues embedded with lots of MXene-derived sheets. In the SEM image for ABS/BODIPY-MXene2.0 (Fig. 9e), it is more clear that the residues are composed of multiple char layers stacked one above the other. Moreover, the wrinkled surface showed in Fig. 9f confirms the carbonization of BODIPY-MXene resulting in the formation of compact and solid char residues. In combination with the LOI test results (Fig. 6), it can be concluded that the chars for ABS/BODIPY-MXene2.0 are more mechanically and thermally stable than that for the other composites, which is more efficient to inhibit the flame spread and molten dripping of ABS.

From XRD patterns (Fig. 10a), it can be seen that the char residues for ABS/BODIPY2.0 are mainly composed of amorphous carbon. For ABS/BODIPY-MXene2.0, the peaks located at 25.5°, 38.0°, 48.0°, 54.6°,

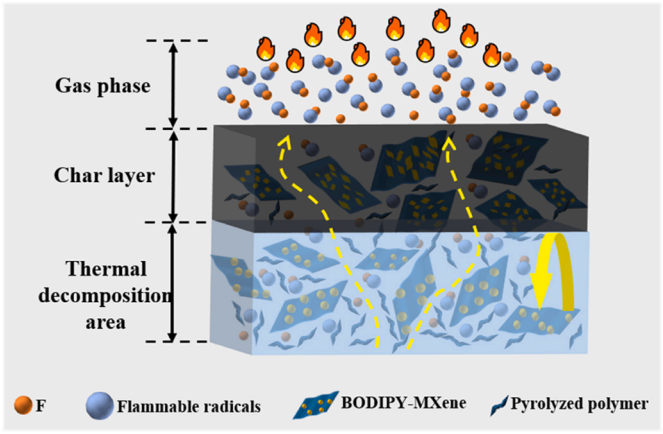

Scheme 2. Illustration of flame retardant mechanism of ABS/BODIPY-MXene nanocomposites.

62.9°, 69.2° and 75.2° are assigned to (101), (004), (200), (211), (204), (220) and (215) diffraction planes for anatase-phase TiO_2, respectively [57]. Except (101) plane, the other diffraction peaks corresponding to TiO_2 are not detected in XRD pattern of ABS/BODIPY-MXene0.5. Because the broad peak at 25.5° also corresponds to amorphous carbon, the char residues for ABS/BODIPY-MXene0.5 and ABS/BODIPY-MXene2.0 are likely a complex composition of TiO_2 nanosheets, amorphous carbon and a few B_2O_3 solids. Fig. 10b exhibits the Raman spectra of the char residues. All the samples show two primary peaks at ca. 1365 cm^{-1} (D band) and 1590 cm^{-1} (G band), which are assigned to amorphous and graphitized carbons, respectively [58]. The graphitization degree of the residues is calculated according to the ratio of the integrated intensities of D/G bands (I_D/I_G), which determines the thermal and mechanical stability of char residues. ABS/BODIPY-MXene0.5 shows the lowest I_D/I_G value (3.14) compared to ABS/BODIPY-MXene2.0 (3.45) and ABS/BODIPY2.0 (3.60) (see Fig. 10b and Fig. S11). It indicates that the presence of BODIPY-MXene can more effectively promote the formation of graphitized carbon than BODIPY. In addition, the peaks appearing at ca. 634, 510, 403 and 155 cm^{-1} are ascribed to the anatase phase of TiO_2 [59], which further confirms the integrated carbon-TiO_2 nanosheets.

Combined with the gas-phase radical reaction, it can be concluded that the "tortuous path" effect caused by the high aspect ratio of uniformly dispersed BODIPY-MXene nanosheets plays an important role in the flammability suppression of ABS (see Scheme 2). The barrier layers provide a reaction room called "micro-reactor" for F atoms and/or HF to capture hydrogen, hydroxide, hydrocarbon and hydro-nitrogen radicals [55]. On the surface of MXene nanosheets, titanium atoms rapidly react with oxygen and/or hydroxide radicals to generate TiO_2, which contributes to the catalytic effect facilitating the delivery of F atoms in the gas phase. In the "micro-reactor", radicals are immobilized to generate carbon particles leading to the soot formation and amorphous and graphitized carbon adhered on the surface of TiO_2 nanosheets. The thermally and mechanically stable char layers prevent the release of flammable and toxic segments decomposed from ABS chains resulting in the reduction in thermal and toxicity hazards.

4. Conclusions

A facile approach for the interface decoration of MXene nanosheets with BODIPY was achieved in this work. The BODIPY-MXene was utilized as a flame retardant additive for ABS resin. Owing to the excellent dispersion of BODIPY-MXene, the addition of 0.5 wt% BODIPY-MXene into ABS resulted in the improvement of the tensile strength (+27.8%), Young's modulus (+18.6%) and elongation at break (+17.9%). The LOI value was increased by 2.0%. Furthermore, the cone calorimeter coupled with FTIR analysis demonstrated the reductions in PHRR (−24.5%), PSPR (−18.4%), peak concentration of HCN (−33.5%), NO (−22.0%), N_2O (−46.6%), NH_3 (−76.0%) and CO (−28.8%). The enhanced fire safety performance of BODIPY-MXene is attributed to the "tortuous path" barrier effect, preventing the combustible gas volatiles and smoke particulate products from migrating onto the polymer surface. The barrier and catalytic effect contributed by MXene nanosheets facilitates the delivery of F atom in the gas phase and prolongs the residence of F atom in the flame zone so that more "hot" radicals are scavenged. Subsequently, the remaining flammable radicals become soot particulates and fixed char residues with TiO_2 nanosheets. The results provide a strong demonstration of the potential future applications of BODIPY-MXene nanosheets as a highly effective flame retardant, toxic fume suppressant and dying agent for polymers.

Declaration of competing interest

The authors declare that they have no known competing financial interests or personal relationships that could have appeared to influence the work reported in this paper.

Acknowledgements

This work was co-financed by National Natural Science Foundation of China (21702042), Anhui Provincial Natural Science Foundation for Distinguished Young Scholar (2008085J26), Anhui Provincial Key Technologies R&D Program (202004a05020044 and 1804a09020070) and Australian Research Council Industrial Transformation Training Center (ARC IC170100032) in the University of New South Wales.

Appendix A. Supplementary data

Supplementary data to this article can be found online at https://doi.org/10.1016/j.compositesb.2021.109130.

Author statement

San-E Zhu: Writing - Original draft preparation, Resources, Conceptualization, Fen-Dou Wang: Experimental, Data curation, Jun-Jie Liu: Investigation, Validation, Li–Li Wang: Data curation, Formal analysis, Cheng Wang: Validation, Data curation, Anthony Chun Yin Yuen: Supervision, Funding acquisition, Visualization, Timothy Bo Yuan Chen: Validation, Data curation, Imrana I. Kabir: Writing - Review & Editing, Guan Heng Yeoh: Writing - Review & Editing, Hong-Dian Lu: Data curation, Formal analysis, Wei Yang: Supervision, Methodology, Project administration, Funding acquisition.

References

[1] Levchik SV, Weil ED. New developments in flame retardancy of styrene thermoplastics and foams. Polym Inter 2008;57:431–48.
[2] Schinazi G, Moraes d'Almeida JR, Pokorski JK, Schiraldi DA. Bio-based flame retardation of acrylonitrile–butadiene–styrene. ACS Appl Polym Mater 2020;3:372–88.
[3] Song P, Cao Z, Meng Q, Fu S, Fang Z, Wu Q, et al. Effect of lignin incorporation and reactive compatibilization on the morphological, rheological, and mechanical properties of ABS resin. J Macromol Sci B 2012;51:720–35.
[4] Prieur B, Meub M, Wittemann M, Klein R, Bellayer S, Fontaine G, et al. Phosphorylation of lignin to flame retard acrylonitrile butadiene styrene (ABS). Polym Degrad Stabil 2016;127:32–43.
[5] Pawlowski KH, Schartel B, Fichera MA, Jäger C. Flame retardancy mechanisms of bisphenol A bis(diphenyl phosphate) in combination with zinc borate in bisphenol A polycarbonate/acrylonitrile–butadiene–styrene blends. Thermochim Acta 2010;498:92–9.
[6] Wang S, Wang S, Hua Y, Zong R, Tang Y, Chen Z, et al. Preparation and characterization of flame retardant ABS/montmorillonite nanocomposite. Appl Clay Sci 2004;25:49–55.
[7] Lu H, Wilkie CA. Synergistic effect of carbon nanotubes and decabromodiphenyl oxide/Sb_2O_3 in improving the flame retardancy of polystyrene. Polym Degrad Stabil 2010;95:564–71.

[8] Li J, Ke C, Xu L, Wang Y. Synergistic effect between a hyperbranched charring agent and ammonium polyphosphate on the intumescent flame retardance of acrylonitrile-butadiene-styrene polymer. Polym Degrad Stabil 2012;97:1107–13.
[9] Zhang Y, Chen X, Fang Z. Synergistic effects of expandable graphite and ammonium polyphosphate with a new carbon source derived from biomass in flame retardant ABS. J Appl Polym Sci 2013;128:2424–32.
[10] Ge L-L, Duan H-J, Zhang X-G, Chen C, Tang J-H, Li Z-M. Synergistic effect of ammonium polyphosphate and expandable graphite on flame-retardant properties of acrylonitrile-butadiene-styrene. J Appl Polym Sci 2012;126:1337–43.
[11] Realinho V, Haurie L, Formosa J, Velasco JI. Flame retardancy effect of combined ammonium polyphosphate and aluminium diethyl phosphinate in acrylonitrile-butadiene-styrene. Polym Degrad Stabil 2018;155:208–19.
[12] Realinho V, Arencón D, Antunes M, Velasco JI. Effects of a phosphorus flame retardant system on the mechanical and fire behavior of microcellular ABS. Polymers 2019;11:30.
[13] Wu N, Li X. Flame retardancy and synergistic flame retardant mechanisms of acrylonitrile-butadiene-styrene composites based on aluminum hypophosphite. Polym Degrad Stabil 2014;105:265–76.
[14] Wu N, Xiu Z. Surface microencapsulation modification of aluminum hypophosphite and improved flame retardancy and mechanical properties of flame-retardant acrylonitrile–butadiene–styrene composites. RSC Adv 2015;5:49143–52.
[15] Hoang D, Kim W, An H, Kim J. Flame retardancies of novel organo-phosphorus flame retardants based on DOPO derivatives when applied to ABS. Macromol Res 2015;23:442–8.
[16] Song W, Zhang W, Li Y, Ma H, Lin T, Lu C, et al. Construction of novel silicon-phosphorus linear polymers with DDSQ and DOPO derivatives for effective flame retardancy of PC/ABS. Fire Mater 2019;43:685–93.
[17] Ma H, Tong L, Xu Z, Fang Z. Clay network in ABS-graft-MAH nanocomposites: rheology and flammability. Polym Degrad Stabil 2007;92:1439–45.
[18] Ma H, Tong L, Xu Z, Fang Z. Synergistic effect of carbon nanotube and clay for improving the flame retardancy of ABS resin. Nanotechnology 2007;18:375602.
[19] He W, Song P, Yu B, Fang Z, Wang H. Flame retardant polymeric nanocomposites through the combination of nanomaterials and conventional flame retardants. Prog Mater Sci 2020;114:100687.
[20] Wu Z, Wang H, Tian X, Ding X, Xue M, Zhou H, et al. Mechanical and flame-retardant properties of styrene–ethylene–butylene–styrene/carbon nanotube composites containing bisphenol A bis(diphenyl phosphate). Compos Sci Technol 2013;82:8–14.
[21] Ma H-Y, Tong L-F, Xu Z-B, Fang Z-P. Functionalizing carbon nanotubes by grafting on intumescent flame retardant: nanocomposite synthesis, morphology, rheology, and flammability. Adv Funct Mater 2008;18:414–21.
[22] Xu S, Zhang L, Lin Y, Li R, Zhang F. Layered double hydroxides used as flame retardant for engineering plastic acrylonitrile–butadiene–styrene (ABS). J Phys Chem Solids 2012;73:1514–7.
[23] Zhang L, Lin Y, Xu S, Li R, Zheng X, Zhang F. Intercalation of perfluorobutane sulfonate into layered double hydroxides. Appl Clay Sci 2010;48:641–5.
[24] Hu D, Zhou Q, Zhou K. Combined effects of layered nanofillers and intumescent flame retardant on thermal and fire behavior of ABS resin. J Appl Polym Sci 2019;136:48220–31.
[25] Hong N, Zhan J, Wang X, Stec AA, Hull TR, Ge H, et al. Enhanced mechanical, thermal and flame retardant properties by combining graphene nanosheets and metal hydroxide nanorods for Acrylonitrile–Butadiene–Styrene copolymer composite. Compos Part A-Appl S 2014;64:203–10.
[26] Huang G, Han D, Jin Y, Song P, Yan Q, Gao C. Fabrication of nitrogen-doped graphene decorated with organophosphor and lanthanum toward high-performance ABS nanocomposites. ACS Appl Nano Mater 2018;1:3204–13.
[27] Huang G, Huo S, Xu X, Chen W, Jin Y, Li R, et al. Realizing simultaneous improvements in mechanical strength, flame retardancy and smoke suppression of ABS nanocomposites from multifunctional graphene. Compos Part B-Eng 2019;177:107377.
[28] Huang G, Chen W, Wu T, Guo H, Fu C, Xue Y, et al. Multifunctional graphene-based nano-additives toward high-performance polymer nanocomposites with enhanced mechanical, thermal, flame retardancy and smoke suppressive properties. Chem Eng J 2021;410:127590.
[29] Ghidiu M, Lukatskaya MR, Zhao MQ, Gogotsi Y, Barsoum MW. Conductive two-dimensional titanium carbide 'clay' with high volumetric capacitance. Nature 2014;516:78–81.
[30] Khazaei M, Arai M, Sasaki T, Chung C-Y, Venkataramanan NS, Estili M, et al. Novel electronic and magnetic properties of two-dimensional transition metal carbides and nitrides. Adv Funct Mater 2013;23:2185–92.
[31] Mashtalir O, Naguib M, Mochalin VN, Dall'Agnese Y, Heon M, Barsoum MW, et al. Intercalation and delamination of layered carbides and carbonitrides. Nat Commun 2013;4:1716–24.
[32] Shi Y, Liu C, Duan Z, Yu B, Liu M, Song P. Interface engineering of MXene towards super-tough and strong polymer nanocomposites with high ductility and excellent fire safety. Chem Eng J 2020;399:125829.
[33] Lu J, Zhang Y, Tao Y, Wang B, Cheng W, Jie G, et al. Self-healable castor oil-based waterborne polyurethane/MXene film with outstanding electromagnetic interference shielding effectiveness and excellent shape memory performance. J Colloid Interface Sci 2021;588:164–74.
[34] Woo JH, Kim NH, Kim SI, Park O-K, Lee JH. Effects of the addition of boric acid on the physical properties of MXene/polyvinyl alcohol (PVA) nanocomposite. Compos Part B-Eng 2020;199:108205.
[35] Aakyiir M, Araby S, Michelmore A, Meng Q, Amer Y, Yao Y, et al. Elastomer nanocomposites containing MXene for mechanical robustness and electrical and thermal conductivity. Nanotechnology 2020;31:315715.
[36] Yu B, Tawiah B, Wang LQ, Yuen ACY, Zhang ZC, Shen LL, et al. Interface decoration of exfoliated MXene ultra-thin nanosheets for fire and smoke suppressions of thermoplastic polyurethane elastomer. J Hazard Mater 2019;374:110–9.
[37] Si JY, Tawiah B, Sun WL, Lin B, Wang C, Yuen ACY, Yu B, et al. Functionalization of MXene nanosheets for polystyrene towards high thermal stability and flame retardant properties. Polymers 2019;11:976.
[38] Yu B, Yuen ACY, Xu X, Zhang ZC, Yang W, Lu H, et al. Engineering MXene surface with POSS for reducing fire hazards of polystyrene with enhanced thermal stability. J Hazard Mater 2021;401:123342.
[39] Xue Y, Feng J, Huo S, Song P, Yu B, Liu L, et al. Polyphosphoramide-intercalated MXene for simultaneously enhancing thermal stability, flame retardancy and mechanical properties of polylactide. Chem Eng J 2020;397:125336.
[40] Tao J, Sun D, Sun L, Li Z, Fu B, Liu J, et al. Tuning the photo-physical properties of BODIPY dyes: effects of 1, 3, 5, 7- substitution on their optical and electrochemical behaviours. Dyes Pigments 2019;168:166–74.
[41] Kamkaew A, Lim SH, Lee HB, Kiew LV, Chung LY, Burgess K. BODIPY dyes in photodynamic therapy. Chem Soc Rev 2013;42:77–88.
[42] Zhu S-E, Zhang J, Dou L, Li N, Hu K, Gao T, et al. Rigid axially symmetrical C_{60}-BODIPY triplet photosensitizers: effect of bridge length on singlet oxygen generation. New J Chem 2020;44:20419–27.
[43] Yan J, Ren CE, Maleski K, Hatter CB, Anasori B, Urbankowski P, et al. Flexible MXene/graphene films for ultrafast supercapacitors with outstanding volumetric capacitance. Adv Funct Mater 2017;27:1701264.
[44] Ghidiu M, Halim J, Kota S, Bish D, Gogotsi Y, Barsoum MW. Ion-exchange and cation solvation reactions in Ti_3C_2MXene. Chem Mater 2016;28:3507–14.
[45] Halim J, Cook KM, Naguib M, Eklund P, Gogotsi Y, Rosen J, et al. X-ray photoelectron spectroscopy of select multi-layered transition metal carbides (MXenes). Appl Surf Sci 2016;362:406–17.
[46] Lin B, Yuen ACY, Li A, Zhang Y, Chen TBY, Yu B, et al. MXene/chitosan nanocoating for flexible polyurethane foam towards remarkable fire hazards reductions. J Hazard Mater 2020;381:120952.
[47] Wang NN, Wang H, Wang YY, Wei YH, Si JY, Yuen ACY, et al. Robust, lightweight, hydrophobic, and fire-retarded polyimide/MXene aerogels for effective oil/water separation. ACS Appl Mater Interfaces 2019;11:40512–23.
[48] Yang W, Liu J-J, Wang L-L, Wang W, Yuen ACY, Peng S, et al. Multifunctional MXene/natural rubber composite films with exceptional flexibility and durability. Compos Part B-Eng 2020;188:107875.
[49] Neher B, Gafur MA, Al-Mansur MA, Bhuiyan MMR, Qadir MR, Ahmed F. Investigation of the surface morphology and structural characterization of palm fiber reinforced acrylonitrile butadiene styrene (PF-ABS) composites. Mater Sci Appl 2014;5:378–86.
[50] Shi Y, Liu C, Liu L, Fu L, Yu B, Lv Y, et al. Strengthening, toughing and thermally stable ultra-thin MXene nanosheets/polypropylene nanocomposites via nanoconfinement. Chem Eng J 2019;378:122267.
[51] Feng J, Carpanese C, Fina A. Thermal decomposition investigation of ABS containing Lewis-acid type metal salts. Polym Degrad Stabil 2016;129:319–27.
[52] Song P, Cao Z, Fu S, Fang Z, Wu Q, Ye J. Thermal degradation and flame retardancy properties of ABS/lignin: effects of lignin content and reactive compatibilization. Thermochim Acta 2011;518:59–65.
[53] Tiganis BE, Burn LS, Davis P, Hill AJ. Thermal degradation of acrylonitrile–butadiene–styrene (ABS) blends. Polym Degrad Stabil 2002;76:425–34.
[54] Yutanova SL, Berezin MB, Semeikin AS, Antina EV, Guseva GB, V'yugin AI. Thermal oxidative degradation of the functionally substituted 2,2′-dipyrrolylmethenes hydrobromides and difluoroborates. Russ J Genl Chem 2013;83:545–51.
[55] Levchik SV. Introduction to flame retardancy and polymer flammability. In: Morgan AB, Wilkie CA, editors. Flame retardant polymer nanocomposites; 2007. p. 1–29.
[56] Wang J, Zhang D, Zhang Y, Cai W, Yao C, Hu Y, et al. Construction of multifunctional boron nitride nanosheet towards reducing toxic volatiles (CO and HCN) generation and fire hazard of thermoplastic polyurethane. J Hazard Mater 2019;362:482–94.
[57] Feng X, Xing W, Song L, Hu Y, Liew KM. TiO_2 loaded on graphene nanosheet as reinforcer and its effect on the thermal behaviors of poly(vinyl chloride) composites. Chem Eng J 2015;260:524–31.
[58] Song S, Ma J, Cao K, Chang G, Huang Y, Yang J. Synthesis of a novel dicyclic silicon-/phosphorus hybrid and its performance on flame retardancy of epoxy resin. Polym Degrad Stabil 2014;99:43–52.
[59] Wang P, Wang J, Wang X, Yu H, Yu J, Lei M, Wang Y. One-step synthesis of easy-recycling TiO_2-rGO nanocomposite photocatalysts with enhanced photocatalytic activity. Appl Catal B-Environ 2013;132–133:452–9.